MITSUBISHI ELECTRIC RESEARCH LABORATORIES
https://www.merl.com

Improving Passenger Comfort by Exploiting Hub Motors in Electric Vehicles: Suspension Modeling

Chen, Di; Danielson, Claus; Masahiro, Iezawa

TR2021-019   March 20, 2021

Abstract

This paper examines using electric vehicles with independently actuated wheels and anti-squat/lift/dive suspensions to improve passenger comfort by reducing the lift, pitch, and roll motion of the vehicle chassis. Anti-squat/lift/dive suspensions use an angled suspension bar to transfer a portion of the longitudinal driving force into a vertical reaction force on the chassis. Using this effect, we derive a control-oriented model of the lift, pitch, and roll of the chassis where the steering angle and the four driving forces of the individual wheels are the control inputs and the road-height is a disturbance. The model is simplified under the assumption that the suspension deflections are small during normal, comfortable driving. Finally, we use steady-state analysis and open-loop simulations to provide intuition about the relationship between the driving forces and the chassis motions.

ASME Dynamic Systems and Control Conference (DSCC) 2020

DSCC2020-XXXX

IMPROVING PASSENGER COMFORT BY EXPLOITING HUB MOTORS IN ELECTRIC VEHICLES: SUSPENSION MODELING

Di Chen
University of Michigan
Email: dichencd@umich.edu

Claus Danielson
Mitsubishi Electric Research Laboratories
Email: danielson@merl.com

Masahiro Iezawa
Mitsubishi Electric Corporation

ABSTRACT

This paper examines using electric vehicles with independently actuated wheels and anti-squat/lift/dive suspensions to improve passenger comfort by reducing the lift, pitch, and roll motion of the vehicle chassis. Anti-squat/lift/dive suspensions use an angled suspension bar to transfer a portion of the longitudinal driving force into a vertical reaction force on the chassis. Using this effect, we derive a control-oriented model of the lift, pitch, and roll of the chassis where the steering angle and the four driving forces of the individual wheels are the control inputs and the road-height is a disturbance. The model is simplified under the assumption that the suspension deflections are small during normal, comfortable driving. Finally, we use steady-state analysis and open-loop simulations to provide intuition about the relationship between the driving forces and the chassis motions.

1 INTRODUCTION

Technologies such as ride-sharing and autonomous vehicles promise to free people from the monotony of commuting. Whether for work or pleasure, many people use this additional free-time to read. However, reading in a moving vehicle can cause motion sickness. Thus, there is renewed interest in developing methods for improving passenger comfort.

This paper examines using anti-squat/lift/dive suspension geometry to actively improve passenger comfort by reducing the lift, pitch, and roll motion of the vehicle. Anti-squat/lift/dive suspensions are a standard feature of modern rear/front/all-wheel drive vehicles [1]. These passive suspensions use an angled suspension arm which redirects a portion of the longitudinal driving force into a vertical reaction force on the chassis that counteracts

the squatting of the rear-end or the lifting of the front-end of the vehicle during acceleration. In vehicles with independently actuated wheel (e.g. electric vehicle with wheel hub motors), we show that we can control these anti-squat/dive/lift forces by intelligently redistributing the controlled driving forces among the four wheels. In other words, we show, independently actuating the wheel throttles can produce the effect of an active suspension without additional hardware. Since the four wheel throttles provide three additional degrees-of-freedom, this improvement in passenger comfort does not compromise the drivability of the vehicle. Specifically, the response of the vehicle to throttle (acceleration) and steering (yaw-rate) commands from the driving (human or autonomous) is unaffected.

The relationship between the longitudinal driving forces and the vertical and rotational motion of the chassis is non-obvious. Thus, this paper derives a control-oriented model that relates the four controlled driving forces to the lift, pitch, and roll dynamics, which determine passenger comfort. In addition, the model includes the yaw dynamics with the steering angle as the fifth control input since differential driving forces will produce a yaw-moment which must be considered. The model also includes the vehicle slip dynamics since the lateral tire forces can induce roll motion on the chassis. A linear model of the tire forces is used since we are considering a passenger vehicle driving under normal conditions. The derived forces that the suspension exerts on the chassis are nonlinear functions of the chassis state, the control inputs, and the road height, which is modeled as an external disturbance. Since we are interested in passenger comfort, we can assume that the vehicle is driven under normal condition resulting in moderate deflection of the suspensions. Thus, we partially linearize the suspension forces. However, the model

remains non-linear due to the slip dynamics and coupling between the steering angle and driving forces for the front wheels. After deriving the model, we perform a steady-state analysis to provide intuition about how the driving forces influence the lift, pitch, and roll motion of the chassis.

Several models [5–8] of hybrid and electric vehicle with four-wheel-drive have been proposed in literature that are capable of describing vehicle's cornering behavior and (or) the roll motion. In [5] and [8], the roll dynamics were derived using a mass-spring-damper model, but the angled suspension arm was omitted. As a result, the anti-squat/lift/dive forces that effect lift, pitch, and roll are not present. The roll model in [6] does not consider the inertia forces during cornering (the center of gravity is assumed to be on the ground) or acceleration (the longitudinal speed of the vehicle is assumed to be constant). [7] is the most relevant work for this paper where the anti-dive/squat forces transmitted from the suspension to the sprung-mass were derived. However, the coupling between the driving forces and the steering angle was not considered. Moreover, the influence of the time-varying road height was not explicitly consider in any of the above-mentioned works. This paper builds on the previous models to derive a new model that includes the lift, pitch, and roll dynamics of the chassis in response to the longitudinal and lateral tire forces, the time-varying road height, and inertia forces due to acceleration and cornering.

We make four contributions to the literature:

1. Our model incorporates the effects of time-varying road-height on the chassis dynamics,
2. Our model considers acceleration and cornering,
3. The complexity of our model is reduced by making several reasonable assumptions for our application,
4. The relation between the state of the sprung-mass and the five control inputs (four driving forces and steering angle) is derived and analyzed to provide intuition about using driving forces to reduce lift, pitch, and roll.

The remainder of the paper is organized as follows: In Section 2, the nonlinear dynamics of the sprung-mass and the suspension assemblies are derived. Afterward, the tire dynamics are discussed and the tire slip angles are derived. In Section 3, the control-oriented model is simplified based on several assumptions, which are reasonable for this application. In Section 4, the nonlinear control-oriented model is analyzed using steady-state analysis and open-loop simulations.

2 Nonlinear Sprung-Mass and Suspension Dynamics

In this paper, passenger comfort is quantified by the lift, pitch, and roll motions of the chassis. Although the spring stiffness is not a control input, passive suspension systems can have geometries that reduce the deflections in the spring length. Following this section, it will be shown that by exploiting the sus-

pension geometry, the motion characterizing passenger comfort can be influenced by the controlled driving forces.

Since any suspension is functionally equivalent to a trailing arm [2], the suspension assemblies can be simplified as trailing arms as shown in Fig. 1. We model the interaction of the suspension assemblies and chassis using reaction forces rather than reaction torque. The spring-damper forces are defined to be in the lift direction. The track width L_j, wheel base b_j as shown in Fig. 1 are assumed to be unchanged ($j = f$ denotes the front suspension, $j = r$ denotes the rear suspension). The left and right side of the vehicle have the same parameter values. Therefore in the sequel we use P_f and P_r to denote the parameter P for the front-right/left or rear-right/left suspension assembly.
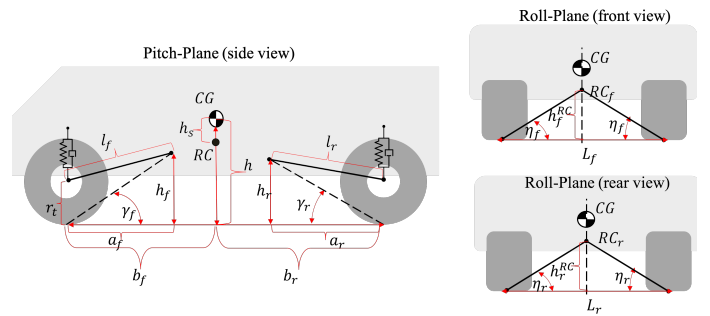

FIGURE 1: Trailing arms and parameter definition in stationary position

2.1 Sprung-Mass Lift, Pitch, Yaw and Roll Dynamics

In this section, we model the lift, pitch, yaw and roll dynamics of the sprung-mass as functions of forces exerted by the four individual suspension assemblies. The front-right (fr), front-left (fl), rear-right (rr) and rear-left (rl) suspension assembly each exert four types of forces on the sprung-mass as shown in Fig. 2:

Spring-damper force F_{sji} induced by the movement of the sprung-mass and the road disturbances.
**Lateral reaction force** F_{yji}^{RC} transferred from (the combined) cornering force to the sprung-mass through the rear-view trailing arm at RC_j.
Longitudinal reaction force F_{xji} transferred from (the combined) driving force to the sprung-mass through the side-view trailing arm at the mounting point.
Vertical reaction forces F_{zji} transferred from (the combined) driving force to the sprung-mass through the side-view trailing arm at the mounting point. F_{zji}^{RC} transferred from (the combined) cornering force to the sprung-mass through the front-view trailing arm at RC_j, respectively.

Here $j \in \{f, r\}$ for front/rear, $i \in \{r, l\}$ for right/left. The same notation will also be used in the sequel. Assuming the left and right suspensions′ pivoting line intersects at the same point, there

is one suspension roll center RC_j for the front/rear suspension assemblies. In addition, the sprung-mass is subject to gravitational force M_sg, inertia force M_sa (when the vehicle is accelerating with a) as well as centrifugal force $M_s\frac{V^2}{R}$ during cornering (when the vehicle is cornering with speed V and radius R) on the center-of-gravity (CG) as shown in Fig. 2. M_s is the sprung-mass mass, and g is the standard gravity constant.
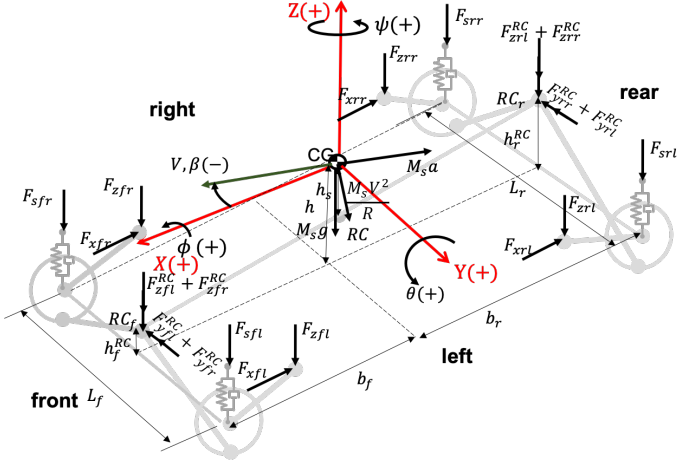
FIGURE 2: Diagram of the forces that the suspensions exert on the sprung-mass. X/Y/Z: longitudinal/lateral/vertical direction in vehicle's inertia frame.

The dynamics of CG in the lift direction are

$$M_s\ddot{z} = -M_sg - \sum_j\sum_i(F_{sji} + F_{zji} + F_{zji}^{RC}), \qquad (1)$$

where z is the lift displacement of CG.

Since this paper considers passenger comfort, vehicle motions in the lift, pitch, and roll directions are small and, as a result the displacement of the CG due to vehicle pitch is small and will be ignore in the rest of the work. The dynamics of the vehicle pitch about CG are

$$
\begin{aligned}
J_Y\ddot{\theta} = &\; F_{sfr}b_f + F_{sfl}b_f - F_{srr}b_r - F_{srl}b_r \\
&+ (F_{xfr} + F_{xfl})(h + z - h_f) \\
&+ (F_{xrr} + F_{xrl})(h + z - h_r) \\
&+ (F_{zfr} + F_{zfl})(b_f - a_f) - (F_{zrr} + F_{zrl})(b_r - a_r) \\
&+ (F_{zfr}^{RC} + F_{zfl}^{RC})b_f - (F_{zrr}^{RC} + F_{zrl}^{RC})b_r,
\end{aligned}
\qquad (2)
$$

where θ is the pitch angle which is defined as the rotation of the sprung-mass about the Y axis, h is the height of CG to the ground when vehicle is stationary, J_Y is the pitch inertia, a_j is the longitudinal distance between the wheel's contact point CP_{ji} and the side-view trailing arm mounting point, h_j is the height of the

side-view trailing arm mounting point to the ground, and a_j and h_j satisfy the following relationship:

$$h_j = a_j\tan\gamma_j, \quad l_j^2 = a_j^2 + (h_j^2 - r_t^2),$$

where l_j represents the fixed length of trailing-arm of front/rear suspension assembly, γ_j represents the anti-dive/squat angle of the side-view trailing arm, and r_t represents the tire radius. Recall that the motions of the sprung-mass are assumed to be small and therefore we assume γ_j, h_j, and a_j are constant.

The ultimate objective is to design a controller that redistributes driving forces to improve comfort without changing the driving characteristics of the vehicle. This requires tracking a reference yaw-rate $\dot{\psi}_r$ provided by the driver, human or autonomous. Thus, our model includes the dynamics of the yaw about the CG given by

$$
\begin{aligned}
J_Z\ddot{\psi} = &\;(-F_{xfr} + F_{xfl})\frac{L_f}{2} + (-F_{xrr} + F_{xrl})\frac{L_r}{2} \\
&- (F_{yfr}^{RC} + F_{yfl}^{RC})b_f + (F_{yrr}^{RC} + F_{yrl}^{RC})b_r,
\end{aligned}
\qquad (3)
$$

where $\dot{\psi}$ is the yaw-rate of the sprung-mass about Z axis and J_Z is the yaw inertia. As will be shown in the subsequent sections, when front wheels are steered or the vehicle has lateral velocity (thus slip angle β), there will be tire slip which induces a cornering force on each wheel. From (3) it should be observed that apart from differential driving forces $F_{xfl} - F_{xfr}$ and $F_{xrl} - F_{xrr}$, difference in cornering forces and the wheel base between the front $(F_{yfr}^{RC} + F_{yfl}^{RC})b_f$ and rear suspension assemblies $(F_{yrr}^{RC} + F_{yrl}^{RC})b_r$ could also induce a yaw torque.

When the vehicle is cornering with speed $V > 0$, and turning radius R, the following relationship between the yaw-rate $\dot{\psi}$ and vehicle slip angle β satisfies

$$
\dot{\beta} = \begin{cases} -\dot{\psi} - \frac{V}{R}, & \delta < 0 \text{ (right turn)} \\ -\dot{\psi} + \frac{V}{R}, & \delta \geq 0 \text{ (left turn)} \end{cases},
$$

or in compact form

$$\dot{\beta} = -\dot{\psi} + \frac{M_s\frac{V^2}{R}}{M_sV}\mathrm{sgn}(\delta), \qquad (4)$$

where the slip angle β is the angle between V and X axis as shown in Fig. 2. Note that $V \neq 0$ when the vehicle is cornering. During cornering, the direction of the centrifugal force changes as the direction of turning changes. Based on our sign convention ($\delta(+)$ for left turn, $\delta(-)$ for right turn), the following lateral force balance needs to be satisfied

$$M_s\frac{V^2}{R}\mathrm{sgn}(\delta)\cos\beta + M_sa_x\tan\beta = -\sum_j\sum_i F_{yji}^{RC}, \qquad (5)$$

where $M_s \frac{V^2}{R}\cos\beta\,\mathrm{sgn}(\delta)$ and $M_s a_x \tan\beta$ are the centrifugal force due to cornering and the inertia force due to acceleration projected onto the lateral direction, respectively.

To prevent changing the driving characteristics of the vehicle, its acceleration a_x should match the reference a_x^r provided by the driver, human or autonomous. The longitudinal acceleration a_x is determined by the force balance in the X-direction

$$M_s a_x = -\sum_j \sum_i F_{xji} + M_s \frac{V^2}{R}\mathrm{sgn}(\delta)\sin\beta.$$

Note that the longitudinal acceleration a_x will also be influenced by centrifugal force $M_s \frac{V^2}{R}$ if vehicle has lateral velocity and thus slip angle β. With (5), the above equation can be simplified as

$$M_s a_x = -\sum_j \sum_i F_{xji}\cos^2\beta - \sum_j \sum_i F_{yji}^{RC}\sin\beta\cos\beta. \tag{6}$$

Note that the desired acceleration a_x^r can be achieved $a_x = a_x^r$ by proper choice of the sum of driving forces $\sum_j \sum_i F_{xji}$.

During cornering, the centrifugal force on CG will cause load transfer to one side of the vehicle. As a result, the vehicle body will roll around the roll axis, which is obtained by connecting RC_f to RC_r as are shown in Fig. 2, and the vehicle body (sprung-mass) rolls around the roll axis. The roll center (RC) as shown in Fig. 2 is the vertical projection of the CG onto roll axis when vehicle is in stationary position. Note that although the roll center and roll axis may change with vehicle movement, in the sequel they are assume to be constant based on our assumption that the lift, yaw and roll motion is small.

For passenger vehicles, the displacement of the CG due to vehicle roll is very small in most cases and can generally be ignored [1]. Thus, the dynamics of the vehicle roll around CG are given by

$$\begin{aligned} J_X \ddot{\phi} = & (F_{sfr} - F_{sfl})\frac{L_f}{2} + (F_{srr} - F_{srl})\frac{L_r}{2} \\ & + (F_{zfr} - F_{zfl})\frac{L_f}{2} + (F_{zrr} - F_{zrl})\frac{L_r}{2} \\ & - (F_{yfr}^{RC} + F_{yfl}^{RC})\big((h+z) - h_f^{RC}\big) \\ & - (F_{yrr}^{RC} + F_{yrl}^{RC})\big((h+z) - h_r^{RC}\big), \end{aligned} \tag{7}$$

where ϕ is the roll angle of the sprung-mass around X axis and J_X is the roll inertia. h_j^{RC} is the RC height of the suspension assembly.

With (5) and (6), the dynamics of the slip β can be simplified as

$$\dot{\beta} = -\dot{\psi} + \frac{\sum_j \sum_i (F_{xji}\sin\beta - F_{yji}^{RC}\cos\beta)}{M_s V_x}, \tag{8}$$

where $V_x = V\cos\beta$ is the vehicle longitudinal velocity and its dynamics are related by

$$\dot{V}_x = a_x, \tag{9}$$

where the longitudinal acceleration a_x is determined by (6).

The state of the sprung-mass is $x = [z, \dot{z}, \theta, \dot{\theta}, \phi, \dot{\phi}, \beta, \dot{\psi}]^T$ where $z, \dot{z}, \theta, \dot{\theta}, \phi, \dot{\phi}$ are included to model performance, β is included due to its influence on the roll ϕ, and $\dot{\psi}$ is included to ensure that the driving characteristics of the vehicle are not changed. From (1), (2), (3) and (7) it can be seen that the dynamics of the lift, pitch, yaw and roll are linear in terms of the suspension forces. However, in the following sections, we will show that the suspension forces are nonlinear functions of the state $x = [z, \dot{z}, \theta, \dot{\theta}, \phi, \dot{\phi}, \beta, \dot{\psi}]^T$, control inputs, and the road disturbances.

2.2 Rear Suspension Forces

In this section we derive the forces that the rear-right and rear-left suspension assemblies exert on the sprung-mass. We assume that the suspension assemblies are at quasi-equilibrium and therefore the forces and torques applied to the suspensions assemblies are balanced [9]. With only front-wheel steering there is no coupling between driving forces u_{ri} and cornering forces n_{ri}.

Fig. 3 shows the side, top and rear views of the free-body diagram of the front-right/left and rear-right/left suspension assemblies. The spring-damper force F_{sri} is given by

$$F_{sri} = -\bar{F}_{sri} + K_r \Delta z_{ri} + C_r \Delta \dot{z}_{ri}, \tag{10}$$

where K_j and C_j denote the spring stiffness and damping coefficient of the suspension assembly, respectively. $\bar{F}_{sji}$ is the static spring force, which can be determined by the force and torque balances in the Z,X,Y-directions

$$\bar{F}_{sfi} = b_r \frac{M_s g}{2\sum_j b_j}, \quad \bar{F}_{sri} = b_f \frac{M_s g}{2\sum_j b_j}. \tag{11}$$

The suspension deflection Δz_{ri} and deflection rates $\Delta \dot{z}_{ri}$ are given by

$$\Delta z_{ri} = z + b_r \tan\theta \mp \frac{L_r}{2}\tan\phi - d_{ri} \tag{12a}$$

$$\Delta \dot{z}_{ri} = \dot{z} + b_r(1 + \tan^2\theta)\dot{\theta} \mp \frac{L_r}{2}(1 + \tan^2\phi)\dot{\phi} - \dot{d}_{ri} \tag{12b}$$

where road height and rate of change in road height at each wheel are denoted by d_{ji} and $\dot{d}_{ji}$, respectively. In (12), $-$ is taken when $i = r$, and $+$ is taken when $i = l$. From (12b) it can be seen
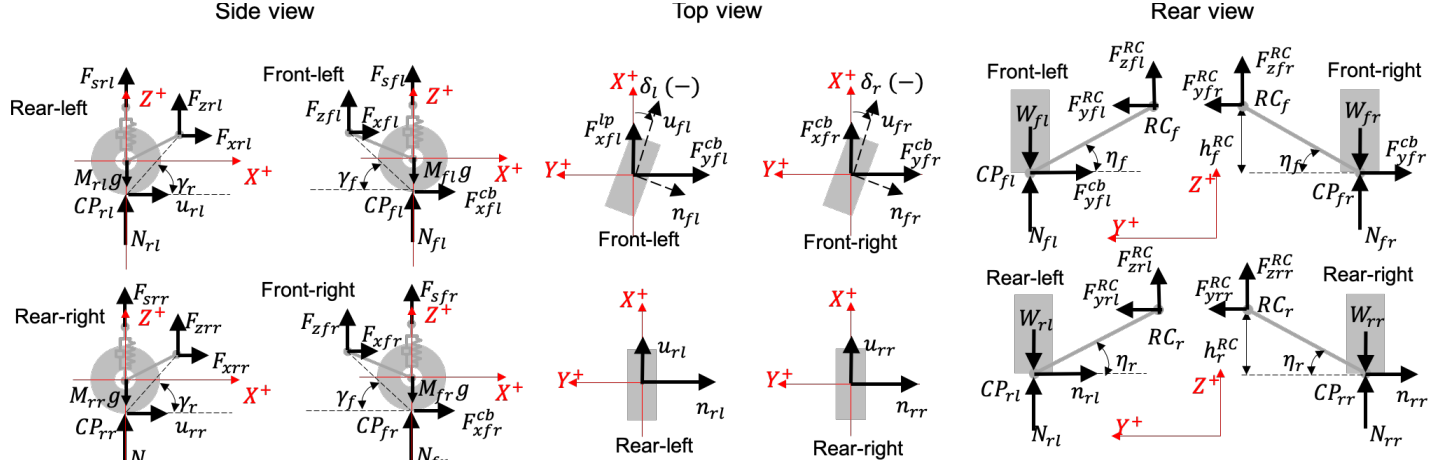
4

FIGURE 3: Free-body diagram of the front and rear suspension assemblies

that the suspension deflection rates are nonlinear functions of the state of the sprung-mass. As a result, the spring-damper forces (10) are nonlinear functions of the state of the sprung-mass.

The force balance in the X-direction and torque balance around tire contact point CP_{ri} (see the side view in Fig. 3) yield the following relationships

$$F_{xri} = -u_{ri} \tag{13a}$$

$$F_{zri} = -u_{ri} \tan \gamma_r. \tag{13b}$$

It can be seen from (13) that the reaction forces in the side view are functions of driving forces. In particular, the force (13b) provides control authority over the lift (1), pitch (2), and roll (7) dynamics. Note that lift reaction force F_{zri} in (13b) is negative when $u_{ri} > 0$ during acceleration, per Newton's third law the lift reaction force that the suspension assembly exerts on the sprung-mass is positive. Thus, the suspension produces an anti-squat reaction force during acceleration and hence this type of suspension is called anti-squat suspension. Similar effects also appears in the front suspension design (anti-dive).

The force balance in the Y-direction and torque balance around tire contact point CP_{ri} yield the following expressions for the roll forces

$$F_{yri}^{RC} = n_{ri}, \tag{14a}$$

$$F_{zri}^{RC} = \pm n_{ri} \tan \eta_r. \tag{14b}$$

where η_j denotes the angle between the trailing arm and the ground in the rear view. In (14b), $+$ is taken when $i = r$, $-$ is taken when $i = l$. Recall that η_j is assumed to be constant since the vehicle motions are small.

It can be seen from (14) that the reaction forces in the rear view are functions of cornering forces n_{ri}. Note that from (14b),

a vertical reaction force will be induced by the cornering force. This explains the source of "jacking" forces inherent to independent suspensions [2]. If the cornering force on the right-side wheel n_{rr} and the left-side wheel n_{rl} has same magnitude, the downward vertical reaction force induced by the cornering force on one wheel will cancel out the lifting effect from the other wheel due to its induced upward vertical reaction force.

The combined driving force u_{ri} and cornering force n_{ri} can not exceed the tire friction limit $\mu_{ji} N_{ji}$, where μ_{ji} and N_{ji} are the friction coefficient and normal force on each tire, respectively. The normal forces on the rear-right/left suspension assembly can be expressed as

$$N_{ri} = M_{ri} g - F_{sri} - F_{zri} - F_{zri}^{RC}, \tag{15}$$

where M_{ri} is the wheel mass of the rear-right/left wheel.

2.3 Front Suspension Forces

The forces produced by the front suspension assemblies differ from the rear due to the steering angle. Since the two front wheels are used for both driving and steering, the longitudinal and lateral forces on the front wheels depend on both the steering angle δ_i and the driving force u_{fi} (see the top view in Fig. 3)

$$F_{xfi}^{cb} = u_{fi} \cos \delta_i + n_{fi} \sin \delta_i \tag{16a}$$

$$F_{yfi}^{cb} = -u_{fi} \sin \delta_i + n_{fi} \cos \delta_i, \tag{16b}$$

where F_{xfi}^{cb} and F_{yfi}^{cb} denote the combined forces in the X and Y-direction, respectively.

With the combined forces (16) in the X (16a) and Y-direction (16b), the modeling of the front suspension assemblies are similar to that of the rear suspension assemblies in the previous section. Similar to (10) and (12), the spring-damper force F_{sfi}, the

suspension deflection Δz_{fi}, as well as the deflection rate $\Delta \dot{z}_{fi}$ are given by

$$F_{sfi} = -\bar{F}_{sfi} + K_f \Delta z_{fi} + C_f \Delta \dot{z}_{fi} \tag{17}$$

$$\Delta z_{fi} = z - b_f \tan \theta \mp \frac{L_f}{2} \tan \phi - d_{fi} \tag{18a}$$

$$\Delta \dot{z}_{fi} = \dot{z} - b_f (1 + \tan^2 \theta) \dot{\theta} \mp \frac{L_f}{2} (1 + \tan^2 \phi) \dot{\phi} - \dot{d}_{fi}, \tag{18b}$$

where the static spring force $\bar{F}_{sfi}$ is given in (11). In (18), $-$ is taken when $i = r$, $+$ is taken when $i = l$.

Unlike the rear suspension assemblies, the reaction forces in the side and rear views are now induced by the combined driving and cornering forces. The force and torque balance (see the side and rear view in Fig. 3) yield the following relationships In the side-view,

$$F_{xfi} = -F_{xfi}^{cb}, \tag{19a}$$

$$F_{zfr} = F_{xfi}^{cb} \tan \gamma_f. \tag{19b}$$

In the rear-view,

$$F_{yfi}^{RC} = F_{yfi}^{cb}, \tag{20a}$$

$$F_{zfi}^{RC} = \pm F_{yfi}^{cb} \tan \eta_f. \tag{20b}$$

In (20b), $+$ is taken when $i = r$, $-$ is taken when $i = l$.

Again, the combined driving force u_{fi} and cornering force n_{fi} are limited by the normal force N_{fi} on each tire. The normal force on the suspension assembly can be expressed according to the force balance in the Z direction

$$N_{fi} = M_{fi} g - F_{sfi} - F_{zfi} - F_{zfi}^{RC}, \tag{21}$$

where M_{fi} is the wheel mass of the front-right/left wheel.

2.4 Linear tire model and cornering forces

Since the vehicle considered is operating under normal driving conditions, a linear model of tire forces is used

$$n_{ji} = C_j^{\alpha} \alpha_{ji}, \tag{22}$$

where C_j^{α} is the cornering stiffness of the front/rear tires. The tire slip angle α_{ji} is the angle between the wheel's velocity vector along the wheel center plane and the vehicle's actual direction of displacement at the tire contact patch [1]. It can be ob-

tained through the rigid body motion and the velocity vector corresponding to each tire [3]

$$\begin{bmatrix} V \cos \beta \\ V \sin \beta \\ 0 \end{bmatrix} + \begin{bmatrix} 0 \\ 0 \\ \dot{\psi} \end{bmatrix} \times \begin{bmatrix} b_f \\ \mp \frac{L_f}{2} \\ 0 \end{bmatrix} = \begin{bmatrix} V_{fi} \cos(\delta_i + \alpha_{fi}) \\ V_{fi} \sin(\delta_i + \alpha_{fi}) \\ 0 \end{bmatrix} \tag{23a}$$

$$\begin{bmatrix} V \cos \beta_i \\ V \sin \beta_i \\ 0 \end{bmatrix} + \begin{bmatrix} 0 \\ 0 \\ \dot{\psi} \end{bmatrix} \times \begin{bmatrix} -b_r \\ \mp \frac{L_r}{2} \\ 0 \end{bmatrix} = \begin{bmatrix} V_{ri} \cos \alpha_{ri} \\ V_{ri} \sin \alpha_{ri} \\ 0 \end{bmatrix}, \tag{23b}$$

where V_{ji} is the speed at the tire contact point of each wheel. In (23), $-$ is taken when $i = r$, $+$ is taken when $i = l$. The first two components in the vector equations (23a) and (23b) offer the relationship among the slip angle, the steering angle and the vehicle slip angle:

$$\tan(\delta_i + \alpha_{fi}) = \frac{V \sin \beta + \dot{\psi} b_f}{V \cos \beta \pm \dot{\psi} \frac{L_f}{2}}, \quad \tan \alpha_{ri} = \frac{V \sin \beta - \dot{\psi} b_r}{V \cos \beta \pm \dot{\psi} \frac{L_r}{2}},$$

where $+$ is taken when $i = r$, $-$ is taken when $i = l$. The above equation leads to the following tire slip angles expressions:

$$\alpha_{fi} = \arctan \left(\frac{V \sin \beta + \dot{\psi} b_f}{V \cos \beta \pm \dot{\psi} \frac{L_f}{2}} \right) - \delta_i \tag{24a}$$

$$\alpha_{ri} = \arctan \left(\frac{V \sin \beta - \dot{\psi} b_r}{V \cos \beta \pm \dot{\psi} \frac{L_r}{2}} \right), \tag{24b}$$

where $+$ is taken when $i = r$, $-$ is taken when $i = l$.

Fig. 4 shows the control inputs and the road disturbances effect the suspension forces which in turn effect the sprung-mass. Recall that the state of the sprung-mass is $x = [z, \dot{z}, \theta, \dot{\theta}, \phi, \dot{\phi}, \beta, \dot{\psi}]^T$, and the suspensions models are quasi-static. As will be discussed and demonstrated through simulations, since the reaction forces are functions of the control input $u = [u_{fr}, u_{fl}, u_{rr}, u_{rl}, \delta]^T$, the behavior of the sprung-mass can indeed be influenced by the considered control input. Meanwhile, to maintain the driving-characteristics, the driving forces must satisfy (6) with $a_x = a_x^r$.

3 Model Linearization for Control Design

From (1)−(3) and (7), the model derived in the previous section is linear with respect to suspension forces, except for the slip angle dynamics (8), where there is nonlinear coupling between the vehicle longitudinal velocity V_x, slip angle β, and the suspension forces. However, the suspension forces (10), (13), (14), (16), (17), (19) and (20) are nonlinear function of the control inputs and the sprung-mass state as shown in (12b), (16) and (18a).
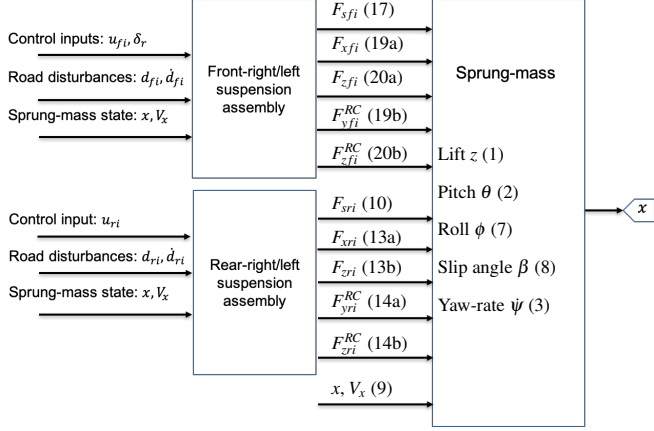
FIGURE 4: Model diagram of the suspension assemblies and the sprung-mass as a dynamic system.

Consequently the relationship from the control inputs and the road disturbances to the sprung-mass state as shown in Fig. 4 is complicated. In addition, the tire slip angles in (24) have nonlinear expressions. For the control design, a simplified model may suffice based on several reasonable assumptions.

3.1 Assumptions for simplification

To simplify the model, we make the following assumptions since the vehicle is under normal driving condition

A.1 Small angle assumption: $\sin \cdot \approx \tan \cdot \approx \cdot$, and $\cos \cdot \approx 1$.
A.2 The steering angles are the same for the front left and right wheels: $\delta_r = \delta_l = \delta$.
A.3 The lift motion z is small compared to the height of CG h ($z \ll h$): $h + z \approx h$.
A.4 The longitudinal velocity is larger compared to the velocity induced by yaw-rate in the longitudinal direction ($V\cos\beta \gg \dot{\psi}\frac{L_f}{2}$, $V\cos\beta \gg \dot{\psi}\frac{L_r}{2}$): $V\cos\beta \pm \dot{\psi}\frac{L_f}{2} \approx V\cos\beta \pm \dot{\psi}\frac{L_r}{2} \approx V\cos\beta$.
A.5 The lateral velocity V_y of the vehicle is small: $V_x \approx V$.

Based on **A.1**, **A.2**, **A.4** and **A.5**, the slip angle of each tire can be simplified from (24) as

$$\alpha_{fi} \approx \beta + \frac{\dot{\psi}b_f}{V_x} - \delta, \quad \alpha_{ri} \approx \beta - \frac{\dot{\psi}b_r}{V_x}. \tag{25}$$

Based on **A.1**, **A.2**, **A.5** and (25), the relationship between a_x and u, x can be simplified as

$$M_s a_x \approx \sum u_{ji} + \sum u_{fi}\delta\beta - 2C_r^\alpha(\beta - \frac{b_r}{V_x}\dot{\psi})\beta$$
$$+ 2C_f^\alpha(\beta + \frac{b_f}{V_x}\dot{\psi} - \delta)(\delta - \beta), \tag{26}$$

where there are no dynamics in a_x. In other words, (26) is an equality constraint on the driving forces u_{ij}.

In addition, based on **A.1** and (25), the normal forces on the rear-right/left wheel (15) is simplified as

$$N_{ri} \approx M_{ri}g + \bar{F}_{sri} - K_r(z + b_r\theta \mp \frac{L_r}{2}\phi - d_{ri})$$
$$- C_r(\dot{z} + b_r\dot{\theta} \mp \frac{L_r}{2}\dot{\phi} - \dot{d}_{ri}) + \tan\gamma_r u_{ri} \tag{27}$$
$$\mp C_r^\alpha(\beta - \frac{b_r}{V_x}\dot{\psi})\tan\eta_r,$$

where $-$ is taken when $i = r$, and $+$ is taken when $i = l$. Likewise, the normal forces on the front-right/left wheel (21) is simplified as

$$N_{fi} \approx M_{fi}g + \bar{F}_{sfi} - K_f(z - b_f\theta \mp \frac{L_f}{2}\phi - d_{fi})$$
$$- C_f(\dot{z} - b_f\dot{\theta} \mp \frac{L_f}{2}\dot{\phi} - \dot{d}_{fi})$$
$$- \tan\gamma_f(u_{fi} + C_f^\alpha(\beta + \frac{b_f}{V_x}\dot{\psi} - \delta)\delta) \tag{28}$$
$$\mp (-u_{fi}\delta + C_f^\alpha(\beta + \frac{b_f}{V_x}\dot{\psi} - \delta))\tan\eta_f,$$

where $-$ is taken when $i = r$, and $+$ is taken when $i = l$.

Based on the above assumptions and linearized expression of tire slip angles (25), the model derived in Section 2 can be simplified for control design. To summarize, the control-oriented model can be written as

$$\dot{x} = f(x, u, d, V_x), \tag{29}$$

where $d = [d_{fr}, \dot{d}_{fr}, d_{fl}, \dot{d}_{fl}, d_{rr}, \dot{d}_{rr}, d_{rl}, \dot{d}_{rl}]^T$. Detailed equations of (29) are omitted here due to space limitation, but can be easily derived from the nonlinear model with the above assumptions **A.1**-**A.5** and the tire slip angles (25).

3.2 Local Controllability of the Control-Oriented Model

The symbolic Jacobian matrices of (29) can be obtained with Matlab Symbolic Math Toolbox:

$$A := \frac{\partial f}{\partial x} = A(x, u, V_x) \tag{30a}$$

$$B_u := \frac{\partial f}{\partial u} = B_u(x, u, V_x), \tag{30b}$$

where the linearized state-space matrices A and B depend inversely $\frac{1}{V_x}$ on the longitudinal velocity. The symbolic controllability matrix $[B_u, AB_u, ..., A^7 B_u]$ has full rank irrespective of

7

the choice of operating conditions ($V_x \neq 0$). Consequently, the nonlinear system (29) is locally controllable at any equilibrium point through the sufficient condition for local controllability at an equilibrium point [4].

4 Open-Loop Simulations

In this section, we analyze how the control inputs influence the sprung-mass motion using the linearized model (30) with a constant driving speed $a_x = 0$ and $V_x \neq 0$. Afterwards, we show that passenger comfort can indeed be influenced by the control inputs using open-loop step responses of both the nonlinear (Fig. 4) and linearized (30) models. In addition, these step responses validate our linearization and steady-state analysis.

Note that in the open-loop simulation, the actual acceleration is obtained from (6). Thus, the control input does not guarantee $a_x = a_x^r = 0$. Consequently, the actual velocity might change as time evolves within each simulation. System parameters used in this work are summarized in Table 1.

TABLE 1: System parameters

L_f [m]	L_r [m]	b_f [m]	b_r [m]	h_f [m]	h_r [m]
1.661	1.699	1.480	1.480	0.3	0.3
h_f^{RC} [m]	h_r^{RC} [m]	$\tan\gamma_f$	$\tan\gamma_r$	$\tan\eta_f$	$\tan\eta_r$
0.1	0.2	0.271	0.309	0.102	0.235
K_f [kN/m]	K_r [kN/m]	C_f [kN/m/s]	C_r [kN/m/s]	C_f^α [kN/rad]	C_r^α [kN/rad]
23	23	1.991	1.991	11	11
M_s [kg]	J_X [kg· m²]	J_Y [kg· m²]	J_Z [kg· m²]		
1822	404	2328	2352		

4.1 Steady-State Analysis with Linearized System

The control-oriented model (29) after simplification is still nonlinear, parameter varying, and has coupling terms between controls and states due to the coupling between the cornering n_{fi} and driving forces u_{fi} on the front wheels. To obtain intuition on the input to output behavior, (29) is linearized at the equilibrium point where the vehicle is driven straight on a flat road at a constant speed $V_{xe} = V_e = 10m/s$. Since we assume the road load has already been balanced by nominal forces and not included in the model and control design, the aforementioned operating condition corresponds to $[u_e, d_e] = [0,0]$, which leads to the following equilibrium point: $[u_e, x_e, d_e] = [0,0,0]$ (therefore $a_{xe} = 0$) from (29) and the corresponding linearized system

$$\dot{x} = A_e x + B_{ue}u + B_{de}d, \tag{31}$$

where $A_e = \frac{\partial f}{\partial x}|_{u_e,x_e,d_e,V_{xe}}$, $B_{ue} = \frac{\partial f}{\partial u}|_{u_e,x_e,d_e,V_{xe}}$, and $B_{de} = \frac{\partial f}{\partial d}|_{u_e,x_e,d_e,V_{xe}}$. Afterwards, the steady-state relationship from the control input u and the road disturbance d to the sprung-mass state x can be obtained through the DC gain analysis. Here we focus on the DC gain matrix G_{yu} from the control input u to

the outputs related to passenger comfort and the driver demand $y = [z, \theta, \phi, \dot{\psi}]^T$.

We use the gain G_{yu} to find input directions that produce decoupled motion as shown in Table 2 and Fig. 5. The corresponding control u is obtained through

$$y^\infty = \begin{bmatrix} G_{yu_1} & G_{yu_2} \end{bmatrix} \begin{bmatrix} u_1^\infty \\ u_2^\infty \end{bmatrix},$$

where $G_{yu} = \begin{bmatrix} G_{yu_1} & G_{yu_2} \end{bmatrix}$, $u_1^\infty = [u_{fr}^\infty, u_{fl}^\infty, u_{rr}^\infty, u_{rl}^\infty]^T$, and $u_2^\infty = \delta^\infty$. The gain G_{yu_1} is of full rank with the linearized dynamics (31), which implies

$$u_1^\infty = G_{yu_1}^{-1}(y^\infty - G_{yu_2}u_2^\infty). \tag{32}$$

TABLE 2: DC gain analysis from control inputs to states for decoupled motion with (31).

z^∞	θ^∞	ϕ^∞	$\dot{\psi}^\infty$	u_{fr}^∞	u_{fl}^∞	u_{rr}^∞	u_{rl}^∞	δ^∞
[m]	[rad]	[rad]	[rad/s]	[kN]	[kN]	[kN]	[kN]	[rad]
0.1	0	0	0	−3.95	−3.95	+4.71	+4.71	0
0	0.1	0	0	−9.13	−9.13	−8.01	−8.01	0
0	0	0.1	0	+3.69	−3.69	−3.62	+3.62	0
0	0	0	0.1	−0.62	+0.62	+0.61	−0.61	0.0255
0	0	0	0.1	−0.47	+0.47	+0.71	−0.71	0

(a) Lift   (b) Pitch   (c) Roll

(d) yaw-rate (steered)   (e) yaw-rate
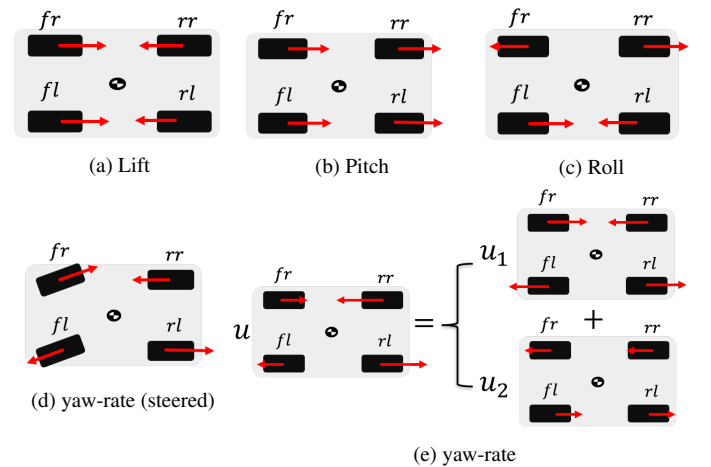
FIGURE 5: Scenarios of decoupled motion from DC gain analysis in Table 2. Red arrows indicate the direction of the driving force on each wheel.

Fig. 5a and the first (non-title) row of Table 2 show the driving forces u_{ij}^{∞} which produce a steady-state lift of $z^{\infty} = 0.1$ meters without any steady-state pitch, roll, or yaw motion when the front wheels are not steered $\delta = 0$. The front wheels have a driving force in the $-X$ and the rear wheels have a driving force in the $+X$ direction. This brings the front and rear wheels slightly closer together, lifting the vehicle due to the angled suspension arms shown in the side view of Fig. 1.

Fig. 5b and the second (non-title) row of Table 2 show the driving forces u_{ij}^{∞} which produce a steady-state pitch $\theta^{\infty} = 0.1$ radians without any steady-state lift, roll, or yaw motion when the front wheels are not steered $\delta^{\infty} = 0$. Both the front and rear wheels have driving forces in the $-X$ direction. Note that this will cause the vehicle to accelerate in the $-X$ direction. This backward acceleration is responsible for the forward pitching of the vehicle, with the anti-lift/squat partially attenuating the natural pitch of the vehicle.

Fig. 5c and the third (non-title) row of Table 2 show the driving forces u_{ij}^{∞} which produce a steady-state roll $\phi^{\infty} = 0.1$ radians without any steady-state lift, pitch, or yaw motion when the front wheels are not steered $\delta^{\infty} = 0$. On the left side of the vehicle, the front and rear wheels have opposing driving forces in the $-X$ and $+X$ directions respectively. This causes the left side of the vehicle to lift. Conversely, on the right side of the vehicle the front and rear wheels have driving forces in the $+X$ and $-X$ directions causing the right side to drop. The result is that vehicle is rolled $\phi^{\infty} = 0.1$ while the net lift of the CG is zero $z^{\infty} = 0$.

Fig. 5d and the forth (non-title) row of Table 2 show the driving forces u_{ij}^{∞} which produce a steady-state yaw $\dot{\psi}^{\infty} = 0.1$ radians per second without any steady-state lift, pitch, or roll motion when the front wheels are have a constant steering angle $\delta^{\infty} = 0.0255$ radians. The steering angle $\delta^{\infty} = 0.0255$ radians produces the desired steady-state yaw rate $\dot{\psi}^{\infty} = 0.1$ radians per second. However, the cornering due to the steered front wheels induces positive roll motion. The control input in the forth (non-title) row of Table 2 is used to counteract this roll motion, resulting in a pure yaw-motion.

Fig. 5e and the fifth (non-title) row of Table 2 show the driving forces u_{ij}^{∞} needed to again produce a decoupled steady-state yaw $\dot{\psi}^{\infty} = 0.1$ when the front wheels are *not* steered $\delta^{\infty} = 0$. The driving forces in the fifth row of Table 2 can be decomposed into two forces u_1 and u_2 as $u = u_1 + u_2$ where the first input u_1 is the previous input from the forth row of Table 2, which counteracts the roll motion induced by the yaw-rate $\dot{\psi}^{\infty} = 0.1$. The second input u_2 is a differential driving force choosen to produce the desire yaw rate

$$u_2 = [0.15, -0.15, 0.10, -0.10, 0]^T.$$

This control input u_2 applies positive (in the $+X$ direction) to the right-side of the vehicle and negative (in the $-X$ direction) to the left-side of the vehicle, producing a net torque in the yaw direction. The input in the fifth row of Table 2 is the sum $u = u_1 + u_2$ of these control inputs.

4.2 Step response to driving forces

To validate the control-oriented model (29), in the following sections, the open-loop step response of the nonlinear system derived in Section 2 is compared to the open-loop simulation result with (29) and the steady-state value obtained from the DC gain calculation with the linearized system (31).

In the first scenario, the vehicle is initially driving at 10 m/s and then constant driving forces are applied the front-right $+161.82N$, front-left $+27.03N$, rear-right $+165.76N$, and rear-left $+297.55N$ wheels from $t = 0$ onward. The steering angle is zero $\delta(t) = 0$ throughout.

The directions of the driving forces are described in Figure. 6a, and the time domain response of the sprung-mass state is shown in Figure. 6b.

The sum of the driving forces is in the $+X$ direction, which corresponds to the case when the vehicle is accelerating, and the driving force on each wheel will induce suspension reaction force (13a), (19a) in the $+X$ direction for each suspension assembly, therefore induce negative motion of the sprung-mass in the pitch direction. However, due to the anti-lift/squat suspension geometries, the driving forces in the $+X$ direction on the two front wheels induce reaction force in the $-Z$ (13b), (19b) direction, and the driving force in the $+X$ direction on the two rear wheels induce reaction force in the $+Z$ direction. The resulting torque in the positive pitch direction will partially attenuate the negative pitch motion caused by the vehicle acceleration. Meanwhile, since the magnitude of the driving forces on the rear wheels are larger compared to those on the front wheels, the $+Z$ lift reaction forces exceed the $-Z$ lift reaction forces. As a result, positive motion of the sprung-mass in the lift direction is induced. In addition, since the driving force on the rear-left wheel is significantly larger than that on the front-left wheel, the large net lift reaction force will be induced in the $+Z$ direction. By comparison, on the right hand side of the vehicle, since the driving forces are similar, the induced lift reaction forces will nearly cancel each other out. Consequently, the resultant will induce positive roll motion of the sprung-mass.

Despite the fact that the actual velocity changes, the linearized control-oriented model (31) is still accurate enough to depict the steady-state of the nonlinear model. In addition, it can be seen that the control-oriented model (29) is a reasonable accurate representation of the nonlinear model.

4.3 Step response to steering angle

Figure. 7 shows the scenario where the steering angle is 0.01 radians (left turn) and the driving forces on each wheel are zero. The time domain response of the sprung-mass state is shown in Fig. 7b.
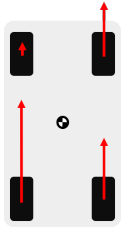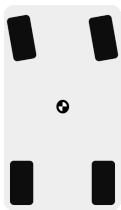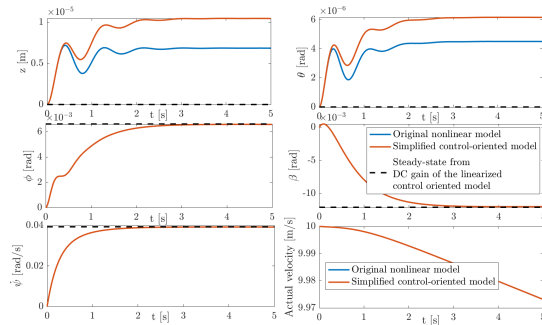
(a) Controls
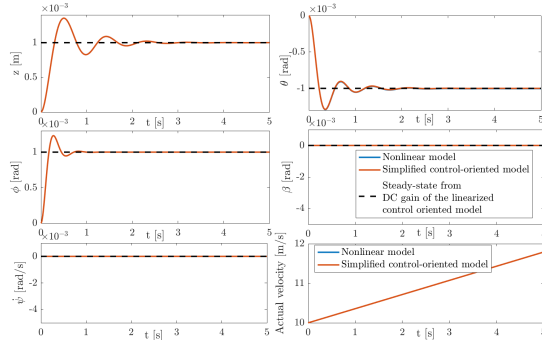
(b) State responses

FIGURE 6: State response comparison among open-loop simulation with the nonlinear model, the control-oriented model and DC gain calculation. Solid blue: open-loop simulation results with nonlinear model. Solid red: open-loop simulation results with (29). Dashed black: DC gain calculation with (31).

(a) Controls

(b) State responses

FIGURE 7: State response comparison among open-loop simulation with the nonlinear model, the control-oriented model and DC gain calculation. Solid blue: open-loop simulation results with nonlinear model. Solid red: open-loop simulation results with (29). Dashed black: DC gain calculation with (31).

Since the vehicle is turning left, the yaw-rate will be positive, and the centrifugal force will cause the vehicle to roll to the right $(+)$ as shown in the third and second subplot in the left column of Fig. 7b, respectively. Note that in the open-loop simulation, although the sum of the driving forces is zero, due to wheel steering, the lateral force will induce forces in the $-X$ direction. Consequently, the actual velocity of the vehicle will decrease.

It can be seen from Fig. 7b that the predicted steady-state with the linearized control-oriented model (31) is accurate enough to depict the steady-state of the nonlinear model except some small errors in the steady-state lift and pitch motion. The discrepancy between the nonlinear and the control-oriented model is small despite some small errors in the lift and pitch motions, which means that the control-oriented model is a rea-

sonable accurate representation of the nonlinear model.

5 CONCLUSIONS

In this paper, we derived a model of the suspension and sprung-mass of electric vehicles with passive suspension and independent wheel drive. We showed, through controllability analysis and open-loop simulations, that the state of the sprung-mass can indeed be influenced by the controlled driving forces. Finally, the effectiveness of the control-oriented model was demonstrated by comparison with the original model in open-loop simulation. It serves as the foundation of the controller design in the subsequent work.

REFERENCES

[1] Heißing, Bernhard, and Metin Ersoy, eds. Chassis handbook: fundamentals, driving dynamics, components, mechatronics, perspectives. Springer Science & Business Media, 2010.

[2] Gillespie, Thomas D. Fundamentals of vehicle dynamics. Vol. 400. Warrendale, PA: Society of automotive engineers, 1992.

[3] Schramm D, Hiller M, Bardini R. Vehicle dynamics. Modeling and Simulation. Berlin, Heidelberg. 2014;151.

[4] Nam K, Arapostathis A. A sufficient condition for local controllability of nonlinear systems along closed orbits. IEEE Transactions on Automatic Control. 1992 Mar;37(3):378-80.

[5] Kim DH, Kim JM, Hwang SH, Kim HS. Optimal brake torque distribution for a four-wheeldrive hybrid electric vehicle stability enhancement. Proceedings of the Institution of Mechanical Engineers, Part D: Journal of Automobile Engineering. 2007 Nov 1;221(11):1357-66.

[6] Ren B, Chen H, Zhao H, Yuan L. MPC-based yaw stability control in in-wheel-motored EV via active front steering and motor torque distribution. Mechatronics. 2016 Sep 1;38:103-14.

[7] Ochi N, Fujimoto H, Hori Y. Proposal of roll angle control method using positive and negative anti-dive force for electric vehicle with four in-wheel motors. In2013 IEEE International Conference on Mechatronics (ICM) 2013 Feb (pp. 816-821). IEEE.

[8] Zendri F, Antonello R, Biral F, Fujimoto H. Modeling, identification and validation of an electric vehicle for model-based control design. In2010 11th IEEE International Workshop on Advanced Motion Control (AMC) 2010 Mar 21 (pp. 118-123). IEEE.

[9] Kim SS, Jeong WH. Real-time multibody vehicle model with bush compliance effect using quasi-static analysis for HILS. Multibody System Dynamics. 2009 Nov 1;22(4):367.